Supporting Information: Membrane Wrapping Efficiency of Elastic Nanoparticles During Endocytosis: Size and Shape Matter

Zhiqiang Shen,[†] Huilin Ye,[†] Xin Yi,[‡] and Ying Li[*,¶]

[†]*Department of Mechanical Engineering, University of Connecticut, Storrs, CT 06269, United States*

[‡]*Department of Mechanics and Engineering Science, College of Engineering, and Beijing Innovation Center for Engineering Science and Advanced Technology, Peking University, Beijing 100871, China*

[¶]*Department of Mechanical Engineering and Institute of Materials Science, University of Connecticut, Storrs, CT 06269, United States*

E-mail: yingli@engr.uconn.edu

Model and Methods

Lipid membrane

One-bead solvent-free lipid model is adopted in our simulations. This highly coarse-grained lipid model can correctly reproduce the dynamic and mechanical properties of lipid membrane.[S1,S2] In this one-bead lipid model, each lipid molecule is represented by a single spherical bead which contains both the translational and rotational degrees of freedom. Conse-

quently, the interactive force between lipid beads depends on both their relative distance r and orientation. The potential function between two beads are given as[S1,S2]

$$U(\mathbf{r}_{ij}, \mathbf{n}_i, \mathbf{n}_j) = \begin{cases} U_{\mathrm{R}}(r) + [1 - \phi(\hat{\mathbf{r}}_{ij}, \mathbf{n}_i, \mathbf{n}_j)], & r < r_{\min}, \\ U_{\mathrm{A}}(r)\phi(\hat{\mathbf{r}}_{ij}, n_i, n_j), & r_{\min} < r < r_{\mathrm{c}}, \end{cases} \tag{1}$$

where $U_{\mathrm{R}}(r)$ and $U_{\mathrm{A}}(r)$ are the distance dependent repulsive and attractive potentials, respectively, $r_{\min}$ is the repulsive force range, and r_{c} is the cutoff distance of the pair-wise interaction. $\phi(\hat{\mathbf{r}}_{ij}, \mathbf{n}_i, \mathbf{n}_j)$ is a weight function to tune the lipid interaction force, where $\hat{\mathbf{r}}_{ij} = \mathbf{r}_{ij}/r$ is the vector direction of the relative distance vector $\mathbf{r}_{ij}$ between two beads, and $\mathbf{n}_i$ and $\mathbf{n}_j$ represent the axes of symmetry of beads i and j, respectively. Specifically, the distance dependent functions are taken as:[S1,S2]

$$\begin{aligned} U_{\mathrm{R}}(r) &= \epsilon[(r_{\min}/r)^4 - 2(r_{\min}/r)^2], && r < r_{\min}, \\ U_{\mathrm{A}}(r) &= -\epsilon \cos^{2\zeta}\left[\frac{\pi(r - r_{\min})}{2(r_{\mathrm{c}} - r_{\min})}\right], && r_{\min} < r < r_{\mathrm{c}}, \end{aligned} \tag{2}$$

where ϵ and σ are the energy and length units, respectively, taken as unity in the simulations. Moreover, $r_{\min} = 2^{1/6}\sigma$ and $r_{\mathrm{c}} = 2.6\sigma$. The repulsive part is the Lennard-Jones (LJ)-42 potential. The attractive part is a cosine function which smoothly connects the repulsive part at $r = r_{\min}$ and decays to zero at the cutoff distance $r = r_{\mathrm{c}}$. ζ is taken as 4 here. The orientation-dependent function is given as[S1,S2]

$$\begin{aligned} &\phi = 1 + \mu[a(\hat{\mathbf{r}}_{ij}, \mathbf{n}_i, \mathbf{n}_j) - 1] \quad \text{with} \\ &a = (\mathbf{n}_i \times \hat{\mathbf{r}}_{ij}) \cdot (\mathbf{n}_j \times \hat{\mathbf{r}}_{ij}) + \sin\theta_0 (\mathbf{n}_j - \mathbf{n}_i) \cdot \hat{\mathbf{r}}_{ij} - \sin^2\theta_0, \end{aligned} \tag{3}$$

where ϕ reaches its maximum of 1 as the angle between two lipid molecules is θ_0. Otherwise, ϕ is less than 1. Here θ_0 is the most energetically favorable angle between two lipids, which is taken as 0 in our simulations. The parameter μ is correlated to the membrane bending rigidity and taken as 3. The temperature of the membrane is controlled at $T = 0.18\epsilon/k_{\mathrm{B}}$,

under which the membrane maintains a fluid state. The membrane tension is maintained at zero by controlling the xy in-plane pressure through a modified Berendsen method.[S3,S4]

Elastic nanoparticles

The elastic NP is modeled by a spherical thin shell consisting of interactive beads as we proposed in our previous work.[S5] These beads locate on a set of evenly distributed vertex points $\underline{\mathrm{x}}_i$ ($i \in 1...N_\mathrm{v}$), which are connected by N_s edges and form N_t triangles on the thin shell. The NP elasticity can be controlled by the area V_area, volume V_volume, in-plane $V_\mathrm{in-plane}$ and bending V_bending potentials. The total potential energy of an elastic NP is defined as

$$V(x_i) = V_\mathrm{area} + V_\mathrm{volume} + V_\mathrm{in-plane} + V_\mathrm{bending}. \tag{4}$$

The in-plane energy $V_\mathrm{in-plane}$ mimics the stretching energy of the elastic networks consisting of harmonic springs

$$V_\mathrm{in-plane} = \Sigma_{j\in 1...N_\mathrm{s}}[k_\mathrm{s}(l_j - l_{j0})^2], \tag{5}$$

where $k_\mathrm{s} = 5\epsilon/\sigma^2$ is the spring constant, l_j is the length of spring, and l_{j0} is the equilibrium length for individual springs.

The area potential V_area is expressed as

$$V_\mathrm{area} = \frac{k_\mathrm{a}(A - A_{T0})^2}{2A_{T0}} + \Sigma_{j\in 1...N_\mathrm{t}}\frac{k_\mathrm{d}(A_j - A_0)^2}{2A_0}, \tag{6}$$

where $k_\mathrm{a} = 0.1\epsilon/\sigma^2$ and $k_\mathrm{d} = 0.08\epsilon/\sigma^2$ are the global area and local area constraints coefficients, respectively; A and A_{T0} are the total area and equilibrium total area, respectively; A_j and A_0 are the area of each triangle and its equilibrium area, respectively. Note that the area potential V_area consists of two parts, the first part controlling the total area of elastic NP and the second part regulating the local area of each triangle.

The in-plane stretching modulus K of the NP shell can be derived as[S6,S7]

$$K = k_{\mathrm{a}} + k_{\mathrm{d}} + \sqrt{3}k_{\mathrm{s}}. \tag{7}$$

Therefore, the in-plane stretching modulus of the elastic NP shell is $K = 8.84\epsilon/\sigma^2$.

The volume potential V_{volume} is expressed as

$$V_{\mathrm{volume}} = \frac{k_{\mathrm{v}}(V - V_{K0})^2}{2V_{K0}}, \tag{8}$$

where $k_{\mathrm{v}} = 1.0\epsilon/\sigma^3$ is the volume constraint coefficient, and V and V_{K0} are the volumes of an elastic NP and its equilibrium value, respectively.

The expression of bending potential V_{bending} is given by

$$V_{\mathrm{bending}} = \Sigma_{j\in 1\ldots N_{\mathrm{s}}} k_{\mathrm{bend}}[1 - \cos(\theta_j - \theta_{j0})], \tag{9}$$

where k_{bend} is the bending constant, θ_j is the dihedral angle between two adjacent triangles sharing the edge j, and θ_{j0} is the corresponding equilibrium dihedral angle. The bending constant k_{bend} is directly related to the macroscopic bending rigidity k_{b} of an elastic NP based on the Helfrich model.[S6,S7] In our simulations, the NP elasticity is controlled by tuning the bending constant k_{bend}.

Calibration of mechanical properties for model membrane

The bending rigidity of the planar membrane can be extracted from the membrane fluctuation spectrum.[S8,S9] Given a membrane profile function $h(x, y)$, its Fourier transform could be expressed as

$$h(q) = \frac{l}{L}\Sigma_n h(\mathbf{r}) \exp(i\mathbf{q}\cdot\mathbf{r}), \tag{10}$$

where L is the lateral side length of the planar membrane. By dividing the membrane into small patches to capture profile function $h(x, y)$, we have the lateral length l of each membrane element. $\mathbf{q} = \frac{2\pi}{L}(n_x, n_y)$ is the wave vector, whose norm is indicated as q. Based on the equipartition theorem, the power spectrum is given as[S10,S11]

$$< |h(q)|^2 >= \frac{k_B T}{l^2[\kappa q^4 + \Sigma q^2]}, \tag{11}$$

where κ and Σ are the bending rigidity and membrane tension, respectively. The membrane bending rigidity κ can be obtained by fitting the measured fluctuation spectrum according to Eq. 11.[S8,S10,S12,S13]

In this numerical study, we built a large flat square membrane of 26569 lipid molecules in the xy-plane. The membrane is relaxed for $2 \times 10^4\tau$ time steps. Afterwards, the membrane is further relaxed with $1 \times 10^5\tau$ time steps for the fluctuation analysis. To measure the out-of-plane fluctuation, the membrane is divided into a 128×128 grid. Therefore, the patch length is $l = L/128$. The average vertical displacement of each patch is recorded to calculate $h(x, y)$. Then we calculate the values of fluctuation spectra by two-dimensional Fourier transform in MATLAB and obtain the membrane bending rigidity as $\kappa = 24\ k_{\mathrm{B}}T$ which falls within the experimental range ($10\ k_{\mathrm{B}}T$–$50\ k_{\mathrm{B}}T$).[S14,S15]

The mean squared displacement of lipid molecules in the xy-plane is also measured during this process. The diffusion coefficient can be calculated as

$$D = \frac{1}{4(t_1 - t_0)} < [\mathbf{r}_{||,i}(t_1) - \mathbf{r}_{||,i}(t_0)]^2 >, \tag{12}$$

where $\mathbf{r}_{||,i}(t)$ is the position of the ith lipid in the xy-plane at time t, and the angular bracket represents an average over all lipids in the membrane. The lipid diffusion constant D is determined as $D = 0.2\sigma^2/\tau$.

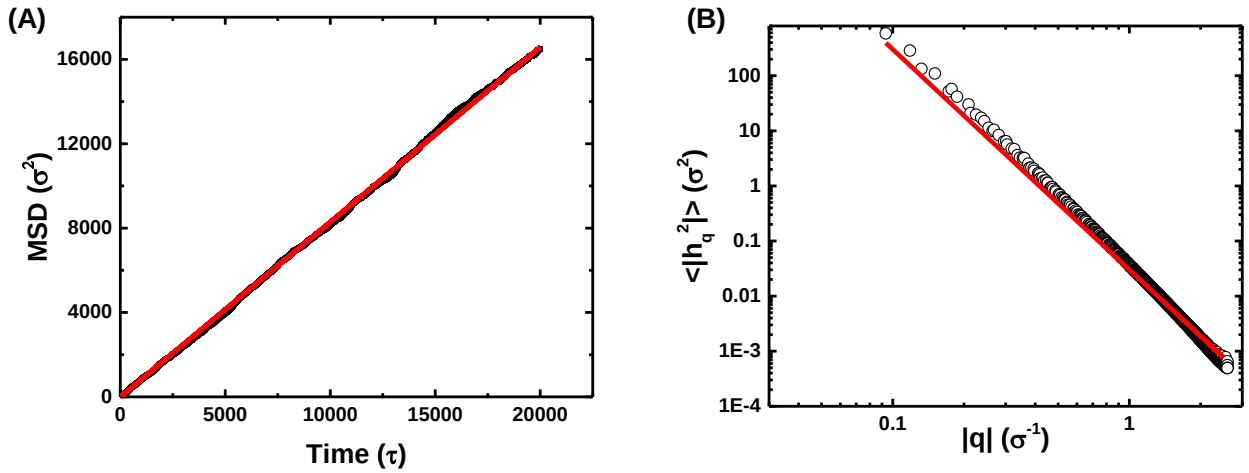

Figure S1: (A) The function of mean squared displacement (MSD) of lipid molecules against time. (B) Out-of-plane fluctuation spectrum of a planar membrane as a function of the wave number q.

Results

Spherical nanoparticles

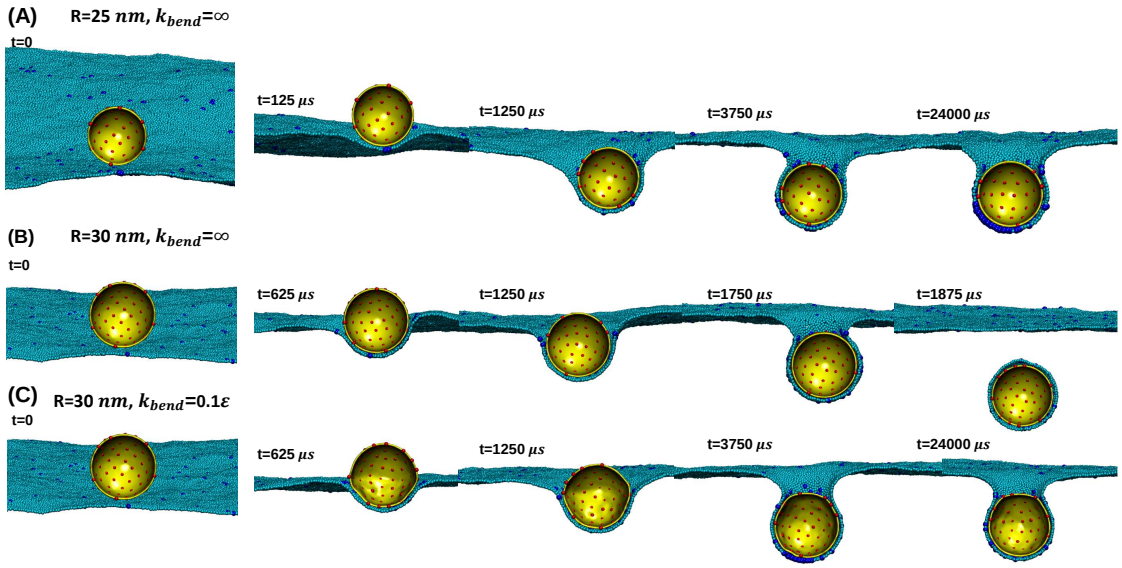

Figure S2: (A) Snapshots of the membrane wrapping of a rigid spherical NP of radius $R = 25$ nm (A) and 30 nm (B). Due to the limited ligand number, the NP of $R = 25$ nm in the case A is trapped during the membrane wrapping process. In contrast, the NP in B can be quickly fully wrapped. (C) Snapshots of the membrane wrapping of a soft spherical NP ($R = 30$ nm) with the bending constant $k_{\text{bend}} = 0.1\epsilon$. Compared to the rigid NP of $R = 30$ nm, the soft NP is trapped owing to the increment of energy barrier.

Computation of membrane bending energy

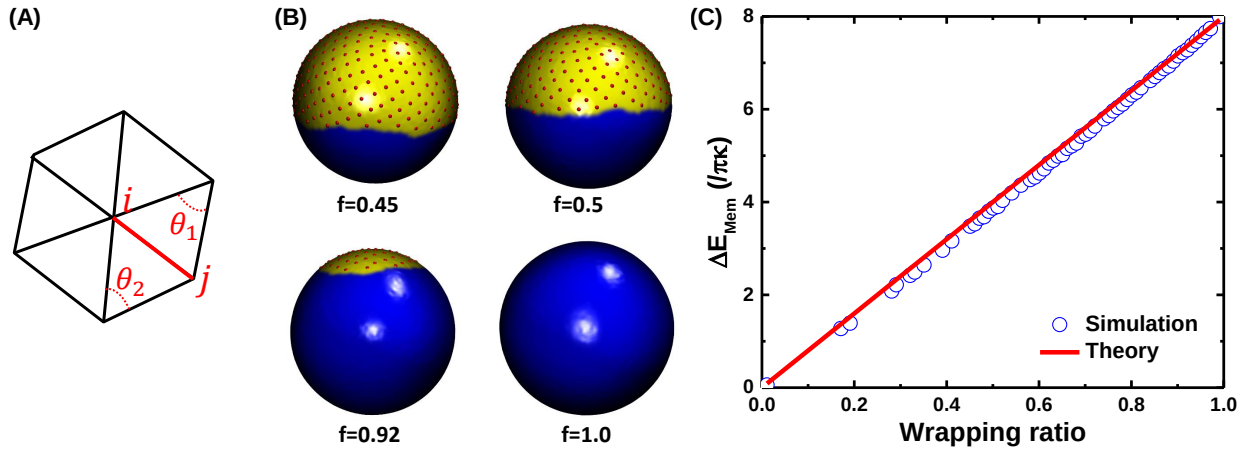

Figure S3: (A) Surface patches of a triangulated NP around vertex i. (B) Evolution of the wrapped part of NPs. The wrapped region of the NP is colored in blue. (C) The comparison between theory and simulation for the membrane bending energy change $\Delta E_{\rm Mem}$ as a function of the wrapping ratio f.

In the wrapped part, the membrane is firmly attached onto the NP surface as shown in Fig. 2 in the main text. Therefore, the membrane bending energy in the wrapped part can be calculated according to the NP curvature as marked in Fig. S3B. For the triangulated NP surface, the mean curvature H at the node i can be calculated as[S16,S17]

$$H = \frac{1}{\sigma_i}\mathbf{n}_i \cdot \Sigma_{j(i)} \frac{\sigma_{ij}}{l_{ij}}(\mathbf{x}_i - \mathbf{x}_j), \tag{13}$$

where $\mathbf{n}_i$ is the surface normal at node i, l_{ij} is the distance between the nodes i and j, and $\sigma_i = \Sigma_{j(i)}\sigma_{ij}l_{ij}/4$ with $\sigma_{ij} = l_{ij}[\cot(\theta_1) + \cot(\theta_2)]/2$. The angles θ_1 and θ_2 are marked in Fig. S3. The summation is conducted over the neighbors of site i.

Then the membrane bending energy can be calculated as[S17]

$$E = \frac{\kappa}{2}\Sigma_i \frac{1}{\sigma_i}\left[\Sigma_{j(i)}\frac{\sigma_{ij}}{l_{ij}}(\mathbf{x}_i - \mathbf{x}_j)\right]^2. \tag{14}$$

As shown in Fig. S3C, our results are in good agreement with the theoretical value $8\pi\kappa f$,[S18] where f is the wrapping ratio.

Deformation of spherical nanoparticles

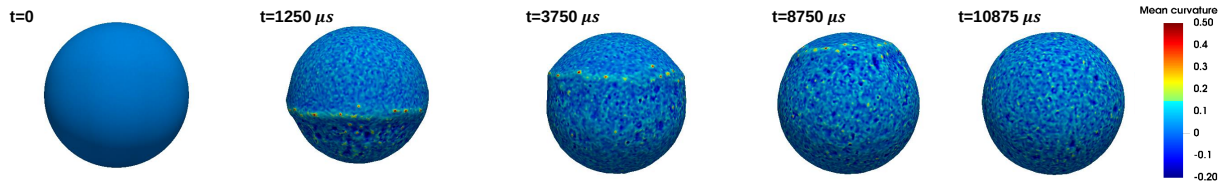

Figure S4: Local curvature field of a soft spherical NP of $k_{\text{bend}} = 0.1\epsilon$ and radius $R = 75$ nm. Corresponding snapshots of the membrane wrapping are given in Fig. 3A in the main text. The color map represents the mean curvature with a unit of nm^{-1}.

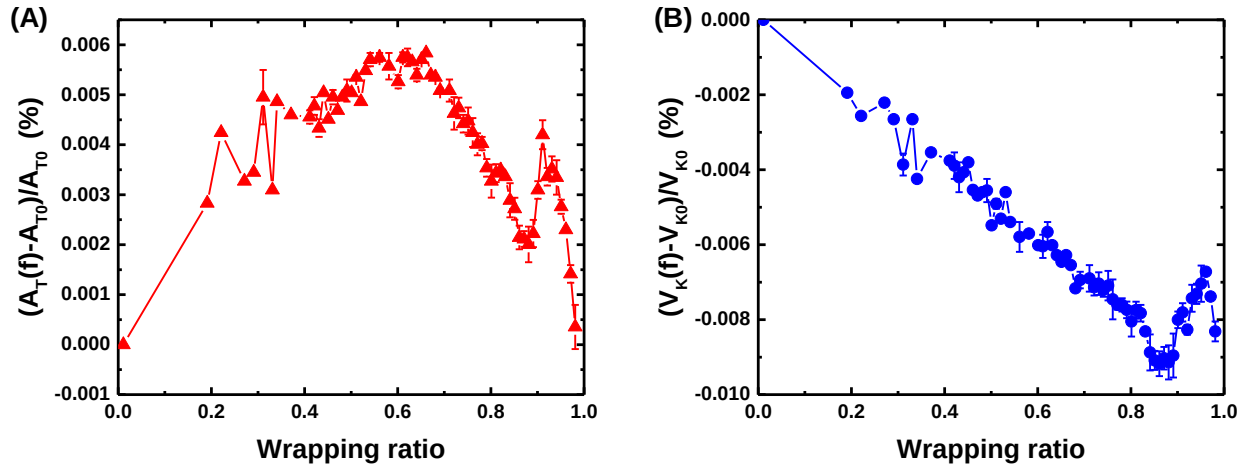

Figure S5: (A-B) The total area and volume variations of the soft spherical NP ($R = 75$ nm, $k_{\text{bend}} = 0.1\epsilon$) as a function of wrapping ratio.

Nonspherical nanoparticles

To analyze the driving force of rotation for both oblate and prolate NPs in simulations, we further compute the membrane energy change of oblate and prolate NPs with the fixed entry angle theoretically. We assume zero membrane tension. For an ellipsoidal NP with a shape function of $(x^2 + y^2)/a^2 + z^2/b^2 = 1$ (a and b are the lengths of half major and minor axes, respectively), the bending energy of the wrapping part can be determined as

$$E_{\text{Bwrap}} = 2\kappa \int M^2(\theta) \mathrm{d}S, \tag{15}$$

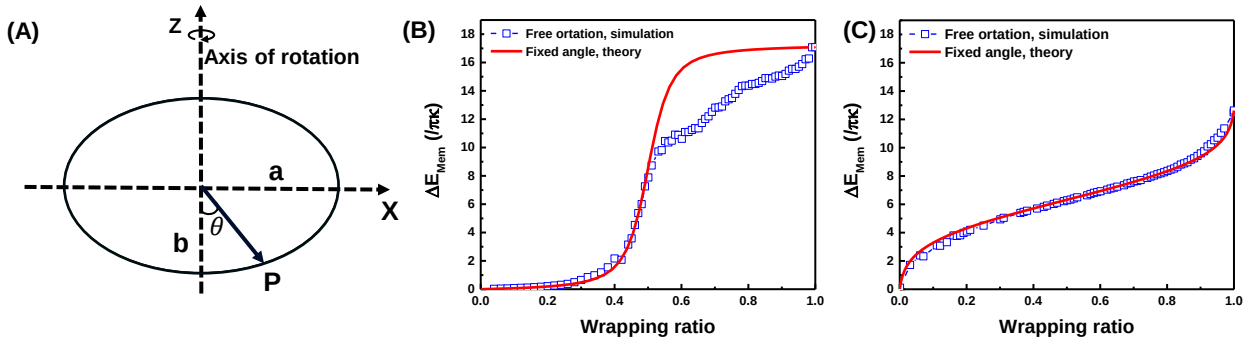

Figure S6: Driving force analysis of NP rotation. (A) Illustration of an ellipsoidal NP. a and b are the lengths of half major and minor axes, respectively. (B) Comparison of the membrane bending energy change for rigid oblate NP in simulation with free rotation and theory with fixed angle. (C) Comparison of the membrane bending energy change for the rigid prolate NP in simulations with free rotation and theory with fixed angle. Corresponding membrane wrapping processes for oblate and prolate NPs are given in Fig. 5 in the main text.

where the mean curvature $M(\theta)$ at the point $\mathrm{P} = (a\sin\theta, -b\cos\theta)$ is given by

$$M(\theta) = \frac{\lambda}{2a}\frac{1+\cos^2\theta+\lambda^2\sin^2\theta}{(\cos^2\theta+\lambda^2\sin^2\theta)^{3/2}} \tag{16}$$

with $\lambda = b/a$. Here the oblate and prolate NPs in theory have the same λ and initial entry angle. The surface area of the wrapped part is $S(\theta) = 2\pi a^2\int_0^\theta \sin\theta'(\cos^2\theta'+\lambda^2\sin^2\theta')^{1/2}d\theta'$.

As shown in Fig. S6, due to the rotation of oblate NP, the associated membrane energy barrier in simulations is smaller than that in theory at a fixed entry angle. It indicates that the membrane bending energy provides the driving force for the oblate NP to rotate. On the other hand, the prolate NP in simulations barely change its orientation. The membrane energy changes in simulations and theory are almost the same.

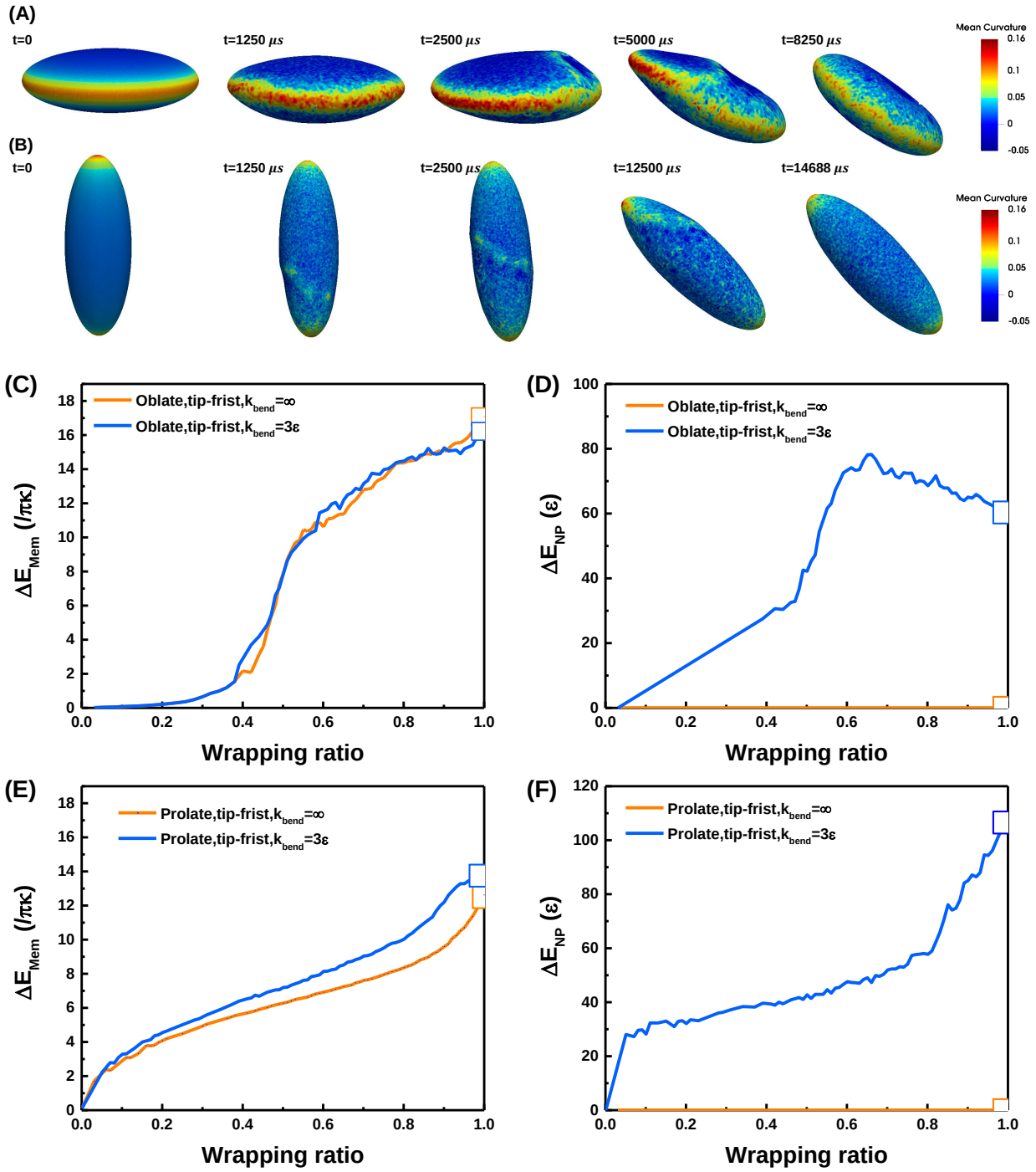

Figure S7: (A-B) Local curvature fields of the soft oblate and prolate NPs with bending constant $k_{\text{bend}} = 3\epsilon$. Corresponding snapshots of the membrane configurations are given in Fig. 7 in the main text. The color map represents the mean curvature with a unit of nm^{-1}. (C-D) Comparisons of membrane energy change and NP energy changes during the membrane wrapping of oblate NPs with $k_{\text{bend}} = \infty$ and $k_{\text{bend}} = 3\epsilon$. (E-F) Comparisons of the membrane energy change and NP energy change during the membrane wrapping of prolate NPs with $k_{\text{bend}} = \infty$ and $k_{\text{bend}} = 3\epsilon$.

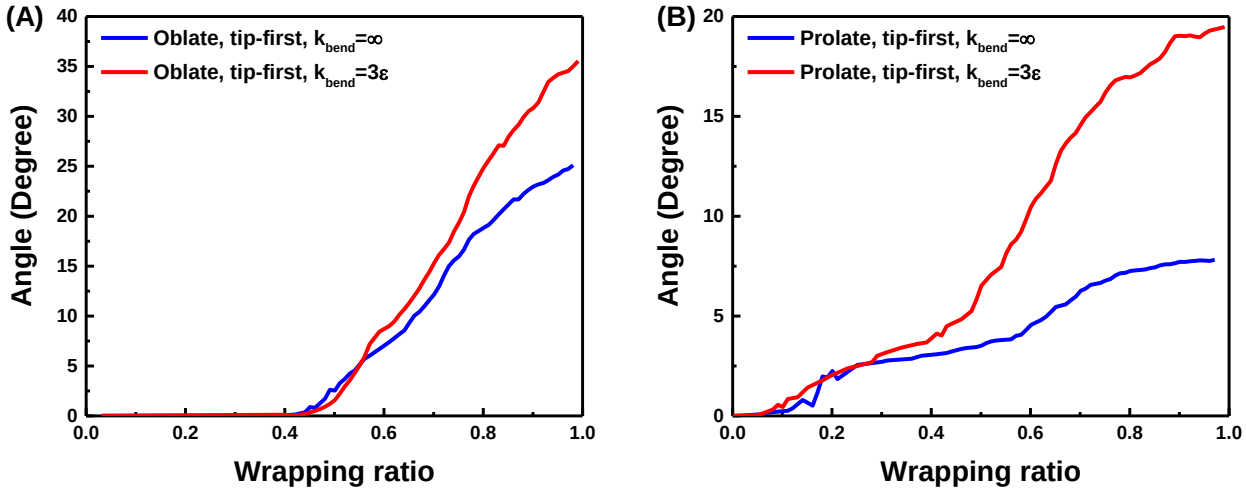

Figure S8: The orientation angle comparison between rigid and soft oblate (A) and prolate (B) NPs with the same entry angle. It is indicated that decreasing the bending constant can promote the NP rotation during the membrane wrapping process. Corresponding snapshots of the membrane configurations are given in Fig. 7 in the main text.

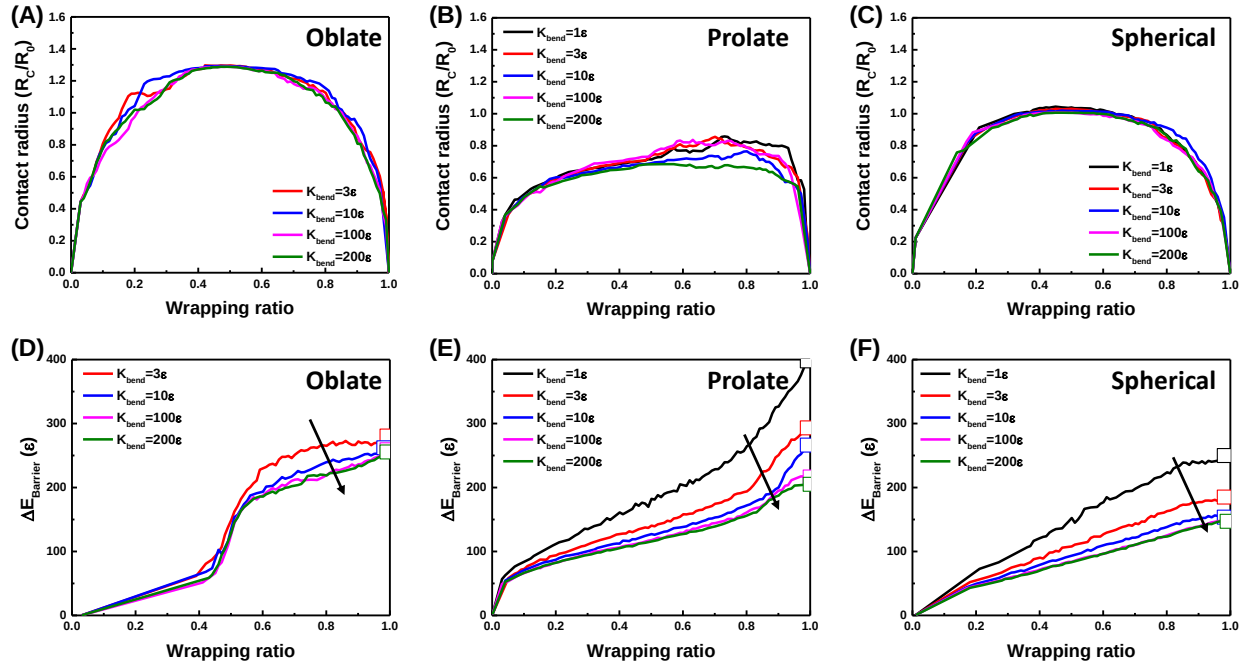

Figure S9: (A-C) Analysis of the contact edge length for oblate, prolate and spherical NPs of different bending constants k_{bend}. (D-F) Analysis of energy barrier for oblate, prolate and spherical NPs of different k_{bend}.

Entry angle influences internalization of nonspherical NPs

As we described above, the membrane wrapping efficiency is determined by the competition between the free energy barrier and contact edge length (or the speed of receptor recruiting). For nonspherical NPs, due to their anisotropic properties, the initial entry angle of both oblate and prolate NPs will affect their contact edge length and energy barrier evolution pathway.[S19–S22] To explore the effect of entry angle, we further study the membrane wrapping process of oblate and prolate NPs ($k_{\text{bend}} = 10\epsilon$) with their minor and major axes parallel to the membrane plane, respectively. We call this wrapping scenario as the side-first entry mode. As shown in Fig. S10, the membrane wrapping pathway is totally different from the tip-first mode for both oblate and prolate NPs with the same bending constant. With the initial small contact area, the oblate NP prefers to lay down first ($1250\ \mu\text{s} < t < 3750\ \mu\text{s}$). It is noteworthy that the oblate NP with the side-first entry mode is less efficient to be wrapped during the entire process than the tip-first entry mode as well as the spherical NP with the same bending constant. In comparison, with the initial large contact area, the prolate NP barely undergoes orientational change during the whole wrapping process. Furthermore, the prolate with the side-first entry mode is much more efficient to be fully wrapped than the tip-first entry mode and the corresponding spherical NP. Intriguingly, with the side-first entry mode, the wrapping efficiency of NPs with the same bending constant is ranked as prolate $>$ spherical $>$ oblate. This ranking sequence is totally reversed for the nonspherical NPs with the tip-first entry mode. These results suggest that the entry angle might be an important factor that contributes to the conflicting experimental results.[S23–S25]

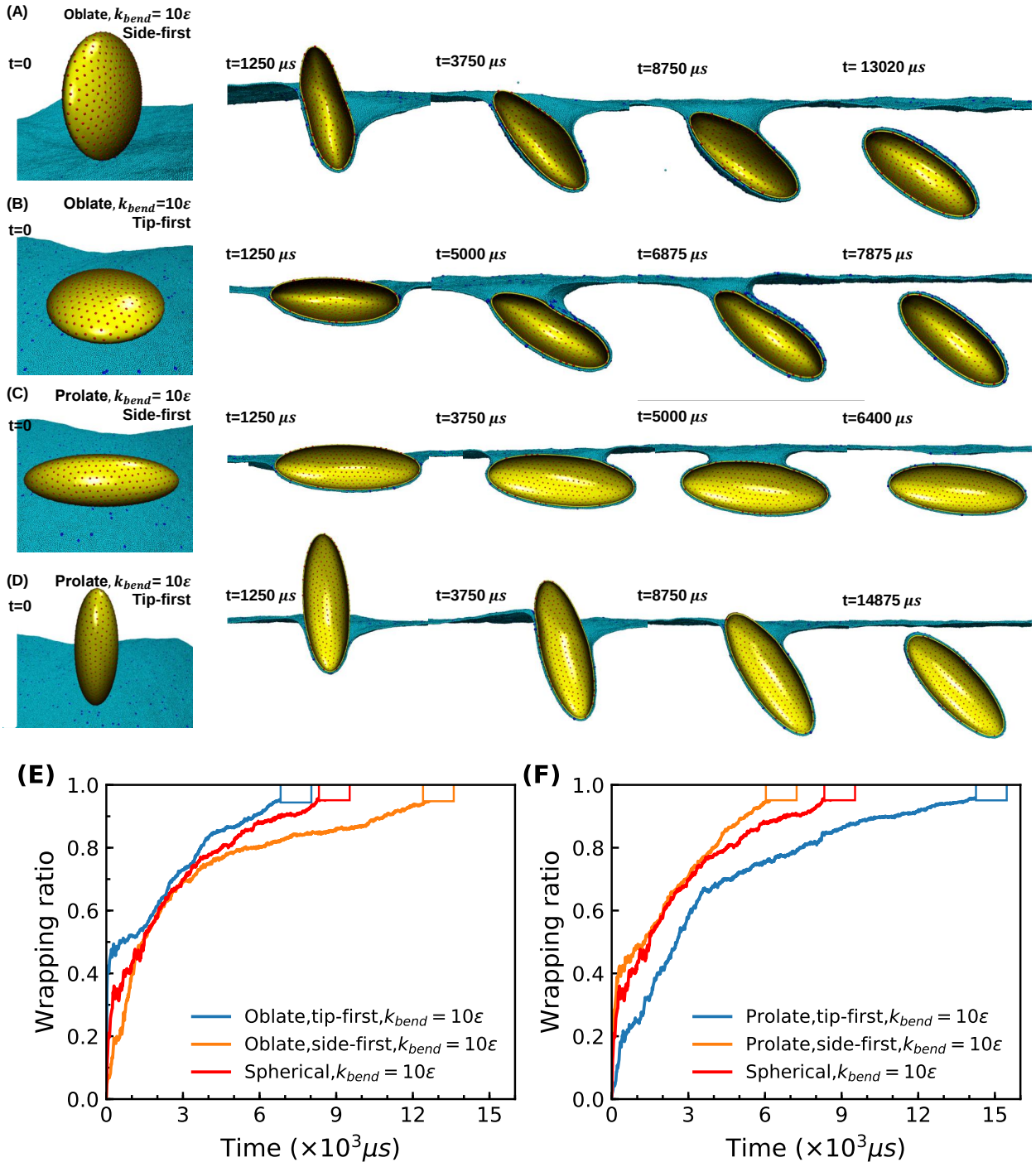

Figure S10: Effects of the entry angle on the wrapping of prolate and oblate NPs. (A-B) The membrane wrapping of soft oblate NPs ($k_{\mathrm{bend}} = 10\epsilon$) with the initially side-first entry mode and tip-first entry mode, respectively. (C-D) The membrane wrapping process of soft prolate NPs ($k_{\mathrm{bend}} = 10\epsilon$) with the initially side-first entry mode and tip-first entry mode, respectively. The wrapping ratios for soft oblate (E) and prolate (F) NPs with tip-first and side-first entry modes.

Cellular uptake of other nonspherical elastic NPs

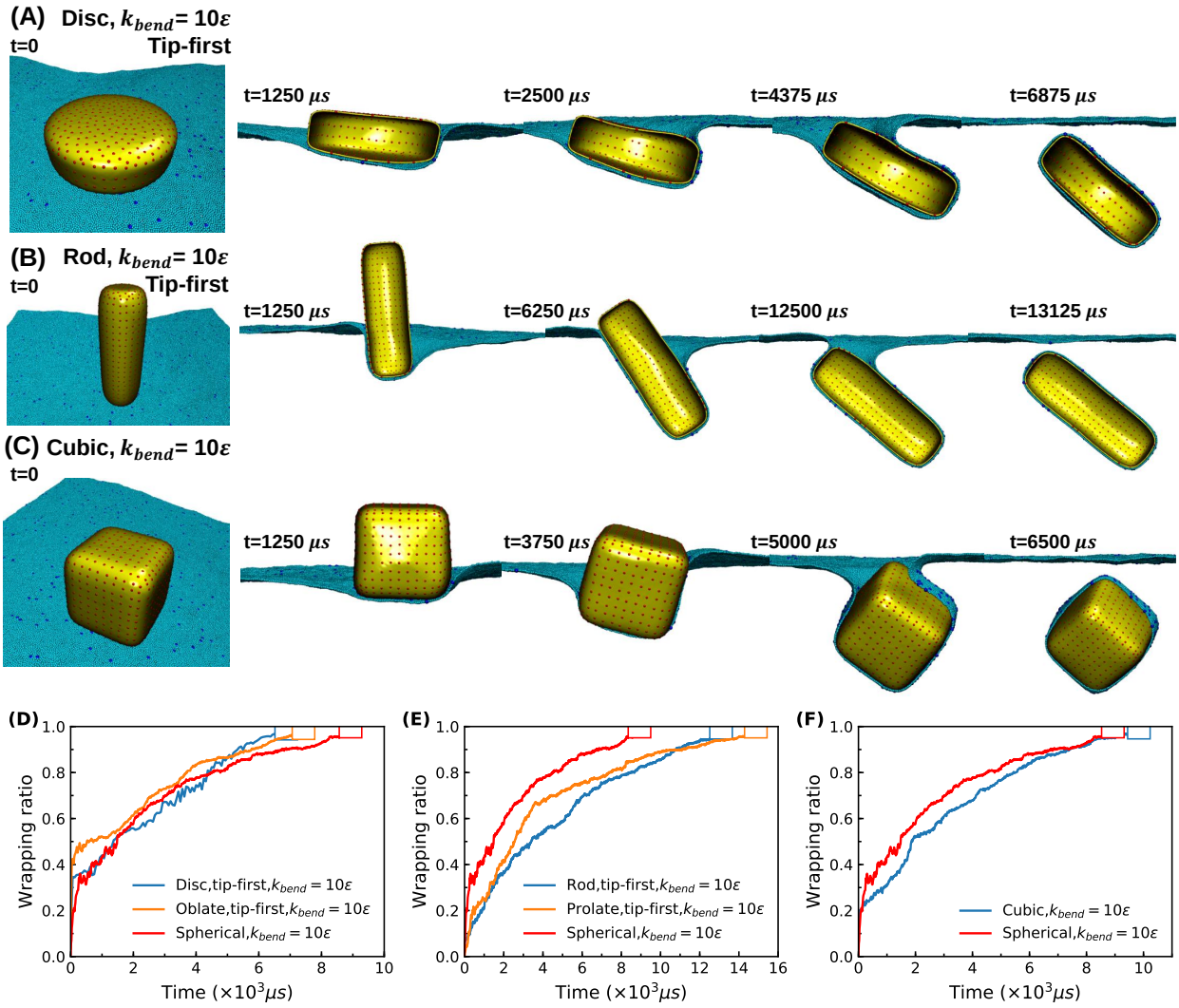

Figure S11: (A-C) Snapshots of the membrane wrapping of soft disc-like, rod-like, and cubic NPs with the bending constant $k_{\text{bend}} = 10\epsilon$. Wrapping ratio comparison between disc-like, oblate and spherical NPs (D), between rod-like, prolate and spherical NPs (E), between cubic and spherical NPs (F).

In experiments, other nonspherical, such as disc, rod-like and cubic NPs are also widely used.[S26–S28] To systematically understand the membrane wrapping behaviors of these nonspherical NPs, we further investigate the membrane wrapping process of soft disc-like, rod-like and cubic NPs at $k_{\text{bend}} = 10\epsilon$. The surface areas of all these NPs are set the same as the spherical NP of radius $R = 75$ nm. The aspect ratio of disc-like and rod-like NPs are

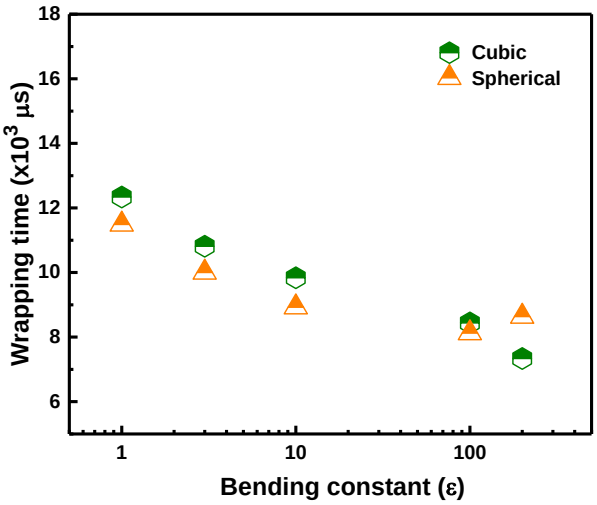

Figure S12: Wrapping time as a function of the bending constant for spherical and cubic NPs.

controlled as the same as the oblate and prolate NPs, respectively. Tip-first entry mode is adopted for disc-like and rod-like NPs. Particularity, we want to explore whether NPs of the same geometric category (one-dimensional shape: rod-like and prolate NPs; two-dimensional shape: disc-like and oblate NPs; three-dimensional shape: cubic and spherical NPs) share the same membrane wrapping pathway and wrapping efficiency. As given in Fig. S11A, the disc-like NP is fully wrapped at $t = 6875$ μs and shares the similar three-stages membrane wrapping pathway as its oblate counterpart in Fig. S10B. Importantly, the wrapping ratio evolutions of disc-like and oblate NPs are similar, and both of them are more efficient to be wrapped than the spherical NP ($k_{\text{bend}} = 10\epsilon$) as shown in Fig. S11D. The rod-like NP lays down gradually as its prolate counterpart does in Fig. S10D, and they share similar wrapping efficiency. Moreover, both of the rod-like and prolate NP are less efficient to be fully wrapped in comparison with the spherical NP (see Fig. S11E). The cubic and spherical NPs share the similar wrapping efficiency (cf. Fig. S11F). Furthermore, the bending rigidity dependent wrapping efficiency of cubic NPs is similar to that of spherical NPs as indicated in Fig. S12. In short, with the tip-first entry mode, the NPs of similar geometry exhibit the similar membrane wrapping pathway and wrapping efficiency. Note that the disc and

rod-like NPs might buckle at $k_{\text{bend}} < 10\epsilon$. Please refer to the method part in the main text for the details about models of disc, rod-like and cubic NPs.

Influence of receptor diffusion flux

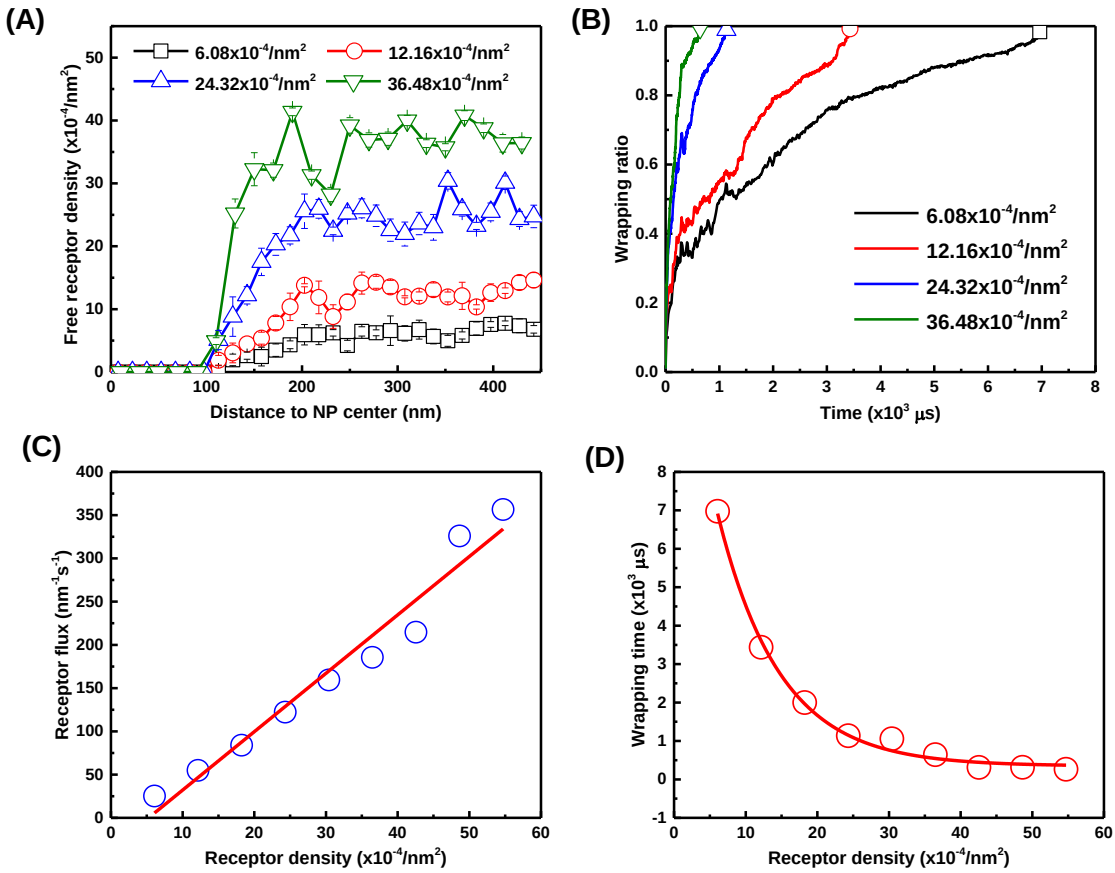

Figure S13: Effects of the receptor diffusion flux on the membrane wrapping of a rigid spherical NP of radius $R = 75$ nm. (A) Densities of the unbounded receptors in the membrane at the wrapping ratio $f = 0.5$. The x-axis represents the distance away from the center of mass of the NP. (B) Corresponding wrapping ratio evolutions at different receptor densities. (C) The relation between receptor diffusion flux and receptor density. The receptor diffusive flux is calculated based on the Fick's first law $J = -D\frac{d\phi}{dx}$, where J is the diffusive flux, ϕ is the receptor density and D is the diffusion coefficient, taken as $D = 5\mu m^2/s$. The slope of $\frac{d\phi}{dx}$ is obtained by fitting the receptor density in the range of 100-200 nm with a linear function. (D) The wrapping time versus the receptor density. The solid line is obtained by fitting the simulation results with an exponential function. The saturation of wrapping time at large receptor densities indicates the elimination of receptor diffusion effect.

References

(S1) Yuan, H.; Huang, C.; Li, J.; Lykotrafitis, G.; Zhang, S. One-Particle-Thick, Solvent-Free, Coarse-Grained Model for Biological and Biomimetic Fluid Membranes. *Phys. Rev. E* **2010**, *82*, 011905.

(S2) Yuan, H.; Huang, C.; Zhang, S. Dynamic Shape Transformations of Fluid Vesicles. *Soft Matter* **2010**, *6*, 4571–4579.

(S3) Guan, Z.; Wang, L.; Lin, J. Interaction Pathways between Plasma Membrane and Block Copolymer Micelles. *Biomacromolecules* **2017**, *18*, 797–807.

(S4) Shi, X.; von Dem Bussche, A.; Hurt, R. H.; Kane, A. B.; Gao, H. Cell Entry of One-Dimensional Nanomaterials Occurs by Tip Recognition and Rotation. *Nat. Nanotechnol.* **2011**, *6*, 714–719.

(S5) Shen, Z.; Ye, H.; Li, Y. Understanding Receptor-Mediated Endocytosis of Elastic Nanoparticles through Coarse Grained Molecular Dynamic Simulation. *Phys. Chem. Chem. Phys.* **2018**, *20*, 16372–16385.

(S6) Fedosov, D. A. Multiscale Modeling of Blood Flow and Soft Matter. PhD Thesis, Brown University, Providence, RI, 2010.

(S7) Fedosov, D. A.; Caswell, B.; Karniadakis, G. E. A Multiscale Red Blood Cell Model with Accurate Mechanics, Rheology, and Dynamics. *Biophys. J.* **2010**, *98*, 2215–2225.

(S8) Cooke, I. R.; Deserno, M. Solvent-Free Model for Self-Assembling Fluid Bilayer Membranes: Stabilization of the Fluid Phase Based on Broad Attractive Tail Potentials. *J. Chem. Phys.* **2005**, *123*, 224710.

(S9) Boal, D.; Boal, D. H. *Mechanics of the Cell, Second Edition*; Cambridge University Press: Cambridge, 2012; p 300.

(S10) Li, H.; Lykotrafitis, G. Two-Component Coarse-Grained Molecular-Dynamics Model for the Human Erythrocyte Membrane. *Biophys. J.* **2012**, *102*, 75–84.

(S11) Helfrich, W. Elastic Properties of Lipid Bilayers: Theory and Possible Experiments. *Z. Naturforsch. C Bio. Sci.* **1973**, *28*, 693–703.

(S12) Fu, S.-P.; Peng, Z.; Yuan, H.; Kfoury, R.; Young, Y.-N. Lennard-Jones Type Pair-Potential Method for Coarse-Grained Lipid Bilayer Membrane Simulations in LAMMPS. *Comput. Phys. Commun.* **2017**, *210*, 193–203.

(S13) Goetz, R.; Gompper, G.; Lipowsky, R. Mobility and Elasticity of Self-Assembled Membranes. *Phys. Rev. Lett.* **1999**, *82*, 221.

(S14) Rawicz, W.; Olbrich, K.; McIntosh, T.; Needham, D.; Evans, E. Effect of Chain Length and Unsaturation on Elasticity of Lipid Bilayers. *Biophys. J.* **2000**, *79*, 328–339.

(S15) Gracià, R. S.; Bezlyepkina, N.; Knorr, R. L.; Lipowsky, R.; Dimova, R. Effect of Cholesterol on the Rigidity of Saturated and Unsaturated Membranes: Fluctuation and Electrodeformation Analysis of Giant Vesicles. *Soft Matter* **2010**, *6*, 1472–1482.

(S16) Guckenberger, A.; Schraml, M. P.; Chen, P. G.; Leonetti, M.; Gekle, S. On the Bending Algorithms for Soft Objects in Flows. *Comput. Phys. Commun.* **2016**, *207*, 1–23.

(S17) David, N.; Tsvi, P.; Steven, W. *Statistical Mechanics of Membranes and Surfaces, Second Edition*; World Scientific: Singapore, 2004; p 383.

(S18) Deserno, M. Elastic Deformation of a Fluid Membrane upon Colloid Binding. *Phys. Rev. E* **2004**, *69*, 031903.

(S19) Dasgupta, S.; Auth, T.; Gompper, G. Shape and Orientation Matter for the Cellular Uptake of Nonspherical Particles. *Nano Lett.* **2014**, *14*, 687–693.

(S20) Li, Y.; Kröger, M.; Liu, W. K. Shape Effect in Cellular Uptake of PEGylated Nanoparticles: Comparison Between Sphere, Rod, Cube and Disk. *Nanoscale* **2015**, *7*, 16631–16646.

(S21) Huang, C.; Zhang, Y.; Yuan, H.; Gao, H.; Zhang, S. Role of Nanoparticle Geometry in Endocytosis: Laying Down to Stand Up. *Nano Lett.* **2013**, *13*, 4546–4550.

(S22) Bahrami, A. H. Orientational Changes and Impaired Internalization of Ellipsoidal Nanoparticles by Vesicle Membranes. *Soft Matter* **2013**, *9*, 8642–8646.

(S23) Sharma, G.; Valenta, D. T.; Altman, Y.; Harvey, S.; Xie, H.; Mitragotri, S.; Smith, J. W. Polymer Particle Shape Independently Influences Binding and Internalization by Macrophages. *J. Controlled Release* **2010**, *147*, 408–412.

(S24) Florez, L.; Herrmann, C.; Cramer, J. M.; Hauser, C. P.; Koynov, K.; Landfester, K.; Crespy, D.; Mailänder, V. How Shape Influences Uptake: Interactions of Anisotropic Polymer Nanoparticles and Human Mesenchymal Stem Cells. *Small* **2012**, *8*, 2222–2230.

(S25) Zhang, Y.; Tekobo, S.; Tu, Y.; Zhou, Q.; Jin, X.; Dergunov, S. A.; Pinkhassik, E.; Yan, B. Permission to Enter Cell by Shape: Nanodisk *vs* Nanosphere. *ACS Appl. Mater. Interfaces* **2012**, *4*, 4099–4105.

(S26) Xia, X.; Yang, M.; Wang, Y.; Zheng, Y.; Li, Q.; Chen, J.; Xia, Y. Quantifying the Coverage Density of Poly (Ethylene Glycol) Chains on the Surface of Gold Nanostructures. *ACS Nano* **2011**, *6*, 512–522.

(S27) Tang, B.; Xu, S.; An, J.; Zhao, B.; Xu, W.; Lombardi, J. R. Kinetic Effects of Halide Ions on the Morphological Evolution of Silver Nanoplates. *Phys. Chem. Chem. Phys.* **2009**, *11*, 10286–10292.

(S28) Huang, X.; Li, L.; Liu, T.; Hao, N.; Liu, H.; Chen, D.; Tang, F. The Shape Effect of Mesoporous Silica Nanoparticles on Biodistribution, Clearance, and Biocompatibility *in Vivo*. *ACS Nano* **2011**, *5*, 5390–5399.